Interface-Driven Chiral Magnetism and Current-Driven Domain Walls in Insulating Magnetic Garnets

Can Onur Avci, Ethan Rosenberg, Lucas Caretta, Felix Büttner, Maxwell Mann, Colin Marcus, David Bono, Caroline A. Ross, Geoffrey S. D. Beach*

Department of Materials Science and Engineering, Massachusetts Institute of Technology, Cambridge, Massachusetts 02139, USA

Magnetic oxides exhibit rich fundamental physics[1–4] and technologically desirable properties for spin-based memory, logic, and signal transmission[5–7]. Recently, spin-orbit-induced spin transport phenomena have been realized in insulating magnetic oxides by using proximate heavy metal layers such as Pt[8–10]. In their metallic ferromagnet counterparts, such interfaces also give rise to a Dzyaloshinskii-Moriya interaction (DMI)[11–13] that can stabilize homochiral domain walls and skyrmions with efficient current-driven dynamics. However, chiral magnetism in centrosymmetric oxides has not yet been observed. Here we discover chiral magnetism that allows for pure spin current-driven domain wall motion in the most ubiquitous class of magnetic oxides, ferrimagnetic iron garnets. We show that epitaxial rare-earth iron garnet films with perpendicular magnetic anisotropy exhibit homochiral Néel domain walls that can be propelled faster than 800 m/s by spin current from an adjacent Pt layer. We find that, despite the relatively small interfacial DMI, very high velocities can be attained due to the antiferromagnetic spin dynamics associated with ferrimagnetic order.

*Author to whom correspondence should be addressed. Electronic mail: gbeach@mit.edu, Phone: +1 617 258-0804

Chiral exchange interactions manifest from broken spatial inversion symmetry. Whereas only a limited number of inversion-asymmetric bulk magnetic materials are known[14–16], engineered interfaces can induce a chiral Dzyaloshinskii-Moriya interaction (DMI) in common centrosymmetric ferromagnets[17–20], in which topological spin textures would otherwise not be found. So far, most research has focused on metallic ferromagnet/heavy-metal bilayers, in which chiral spin textures can be stabilized by interfacial DMI at room temperature[21–23]. Such systems simultaneously benefit from the large spin Hall effect present in DMI-inducing heavy metals like Pt, which provides a source of pure spin current to manipulate chiral spin textures efficiently[21,24].

Due to their chemical and structural complexity, magnetic oxides exhibit a broader range of exotic and useful properties than metals, and oxide-based spintronics may permit functionalities not otherwise readily achieved[4,5,7]. Insulating magnetic oxides are of particular interest due to their low damping, large magnon diffusion length, and the possibility to generate and transmit pure spin currents with minimal dissipation[6,9]. However, realization of chiral spin textures in magnetic oxides remains a challenge, as few bulk chiral magnetic oxides are known[16]. Interface-induced DMI in centrosymmetric oxides has so far only been studied in conducting oxides at cryogenic temperatures[25–27], using indirect magneto-transport measurements whose interpretation can be ambiguous[28,29].

In this work, we characterize pure spin current-induced domain wall (DW) motion in insulating rare-earth iron garnet films capped by Pt, revealing an interfacial DMI at room temperature whose strength we quantitatively deduced from the dynamics. Experiments examined perpendicularly-magnetized 5-7 nm thick $Tm_3Fe_5O_{12}$ (TmIG) and $Tb_3Fe_5O_{12}$ (TbIG) films grown epitaxially on (111)-oriented $Gd_3Ga_5O_{12}$ substrate and covered by a 4 nm-thick Pt layer (see Methods). DW motion was studied in lithographically-patterned tracks (Fig. 1a) with contacts at either end for current injection and with an orthogonal Au wire for domain

nucleation (see Methods). Lateral voltage contacts were included for Hall resistance measurements. Magnetization reversal was detected locally using a scanning magneto-optical Kerr effect (MOKE) polarimeter with a focused laser spot size of ~5 μm.

Figure 1 summarizes magneto-transport and magnetic switching measurements used to characterize spin transport across the Pt/TmIG interface. Figure 1b shows Hall resistance R_H versus in-plane field H oriented 45° from the injected current density j (Methods). The $\sin^2\theta$ dependence arises from the spin Hall magnetoresistance (SMR)[8], with θ the azimuthal angle of the (normalized) magnetization vector **m**, which rotates from out-of-plane to in-plane as H increases. From the amplitude change $\Delta R_H = R_{SMR} \cong 8.1$ mΩ and the measured sheet resistance $R_\square = 75\ \Omega$, we find a SMR ratio $R_{SMR}/R_\square \cong 1.1 \times 10^{-4}$ indicative of a large spin-mixing conductance, similar to previous reports[10]. The imaginary part of the spin-mixing conductance leads to an additional anomalous Hall-like SMR contribution to R_H that tracks the out-of-plane magnetization[10], as seen in the hysteresis loops in Fig. 1c. This contribution gives rise to the hysteretic behavior around zero field in Fig. 1b, due to slight misalignment of H relative to the sample plane. Finally, Fig. 1d demonstrates spin Hall current-induced switching of the TmIG magnetization in the presence of a longitudinal field H_x detected by both Hall effect and MOKE measurements. The small switching current density implies a large damping-like torque reflecting the large spin Hall effect in the Pt layer combined with significant interfacial spin transparency. The damping-like torque effective field H_{DL} was quantified using harmonic measurements (see Supplementary Information), yielding an effective spin Hall angle $\theta_{SH}^{eff} \sim 2\%$, consistent with prior reports[10].

Figure 2a shows time-resolved MOKE transients measured at several positions along the track in Fig. 1a during field (H_z)-driven motion of a DW initialized near the DW nucleation line (see Methods). The locally-probed magnetization switching time increases linearly with

increasing distance from the nucleation line (Fig. 2b), confirming reversal by a single propagating DW. The average DW velocity v follows the usual creep scaling $\ln v \propto H_z^{-1/4}$ in this low-field regime (Fig. 2c), indicating propagation through a weak disorder potential.

We quantified the current-induced effective field acting on DWs by measuring its influence on DW propagation[12]. The current-induced effective field manifests as a variation in the DW propagation field H_p under d.c. current injection[12,30]. H_p was extracted from hysteresis loops (Fig. 3a) in which DWs were controllably nucleated during one half of the field-sweep cycle, such that the switching field corresponds to the field required to depin the nucleated DW. The linear relative change in the propagation field $\Delta H_p \propto j$ (Figs. 3a,b), indicates that current generates an effective out-of-plane field $|H_{eff}/j| \approx 15.5 \pm 1.2$ Oe per 10^{11} A/m^2, which assists DW propagation in the electron flow direction. This result is in quantitative agreement with harmonic measurements of the damping-like torque (see Supplementary Information).

Damping-like torque manifests as a z-axis effective field $H_{eff} = \frac{\pi}{2} H_{DL} \cos(\psi)$ in a DW, with ψ the angle between the DW moment and the x-axis. Figure 3b hence implies that the DWs are Néel type ($\psi = 0, \pi$) and that up-down and down-up DWs have oppositely-oriented moments since H_{eff} is of opposite sign. This suggests a chiral exchange field H_{DMI} that stabilizes homochiral Néel DWs in this system. To confirm this, we measured the dependence of the critical depinning current j_{crit} on longitudinal field H_x (see Methods). j_{crit} represents the threshold at which H_{eff} overcomes the effective pinning field, and it should hence vary with ψ. Figure 3c shows that for down-up DWs, j_{crit} is unchanged for $H_x > 0$, diverges near $H_x \sim -50$ Oe, and changes sign across this threshold. Up-down DWs exhibit similar behavior, with the signs of j and H_x inverted. This can be understood from the schematics in Fig. 3d. For down-up walls, the DW moment orients to the right at zero field and rotates from Néel to Bloch to Néel with opposite chirality under increasing $H_x < 0$. H_{eff} has opposite signs for oppositely-

oriented Néel DWs and vanishes for Bloch DWs, leading to the observed behavior of j_{crit} versus H_x. As shown in Fig. 3c, the data are well-fitted by a simple model in which j_{crit} scales as $1/H_{eff}$ and ψ follows the usual one-dimensional DW model[30]. We find a chiral exchange field $|H_{DMI}|$ ≈ 47 Oe corresponding to an interfacial DMI constant $|D|$ ≈ 0.002 mJ/m^2 (see Supplementary Information). Normalized to the film thickness, D is nearly two orders of magnitude lower than in Pt/metallic-ferromagnet systems. However, since the threshold DMI strength (D^{th}) required to stabilize Néel DWs[31] scales as the DW demagnetizing energy, $|D^{th}| = (2t\ln(2)/\pi^2)\mu_0 M_s^2$ (here t is the magnetic layer thickness), the threshold required for Néel DWs in these low-M_s garnets is a factor of ~10^2 smaller than a 1 nm-thick Co film.

Pt is known to induce strong DMI at Pt/ferromagnetic-metal interfaces, but the chirality in all previously-studied systems is left-handed when the Pt layer is underneath ferromagnetic metal, i.e., on the substrate side[32]. Surprisingly, the DWs in this system are also left-handed despite the fact that Pt is on top of the magnetic layer meaning that they have the opposite chirality relative to that induced by Pt in all previously studied systems. This is evidenced by the in-plane field dependence in Fig. 3 and the fact that DWs move in the electron flow direction, opposite to that in metallic systems such as Pt/Co. To gain more insight into the origin of the chiral effective field, we varied the rare-earth ion in the garnet and the interface between the garnet and the Pt. Figure 4 shows ΔH_p versus j, measured as in Figs. 3a,b, for up-down DWs in TmIG/Pt, TbIG/Pt, and TbIG/Cu(2nm)/Pt under various H_x. We see that in all cases DWs move against current flow at zero H_x, and under $H_x < 0$ the slope of ΔH_p versus j inverts. This implies that all three systems share the same chirality with similar H_{DMI} strength, since the field at which H_{eff} vanishes and DWs become Bloch is similar. We finally estimate $|D|$≈0.0014 mJ/m^2 for the TbIG samples which, scaled by thickness, implies nearly the same interfacial DMI energy as for TmIG (see Supplementary Information). In this case, there is no measurable change in the chiral exchange field.

If Pt were responsible for the interfacial DMI, then inserting a Cu spacer should significantly decrease its strength. Comparison between Figs. 3b and c show this is not the case. It is known from previous works that adding even a few Å dusting layer between Pt and the ferromagnet is sufficient to entirely quench interfacial DMI[11,24]. The observation that insertion of 2 nm of Cu between Pt and the TmIG produces no measurable change in DMI indicates strongly that DMI is not induced by the Pt. The fact that the 2 nm Cu layer does change dramatically the damping-like torque at this interface in our experiment confirms that it is thick and continuous enough to change the nature of the interface itself. On the other hand, if bulk-like contributions played a role, one may expect a dependence on the heavy rare-earth ion, whose orbital moment is different for Tm and Tb, but this also is not observed. Moreover, cycloidal order (Néel textures) require a form of DMI associated with broken inversion symmetry at a surface, not in the bulk[17]. Since the DMI is insensitive to the top interface and occurs generally in these rare-earth garnets, the substrate oxide/magnetic oxide interface may instead play the dominant role. Rashba splitting is known to manifest at oxide-oxide interfaces[2,33] such as $LaAlO_3/SrTiO_3$, which exhibit a variety of emergent two-dimensional magnetic phenomena[4]. Rashba-generated DMI has recently been predicted at oxide-oxide interfaces[3,34], and Rashba-induced DMI can occur even in materials lacking strong spin-orbit coupling[20]. A more systematic study of the dependence of the DMI on garnet thickness, rare-earth ion, crystallographic orientation, and substrate lattice mismatch could shed light into the origins of the interfacial DMI observed in this system.

Finally, we characterized high-speed DW dynamics driven by short current pulses (see Methods). Fig. 5a shows DW velocity v as a function of j in TmIG/Pt. We observe velocities exceeding 800 m/s at $j = 1.2 \times 10^{12}$, and a depinning threshold at $j \cong 0.4 \times 10^{11}$ A/m^2, which is about an order of magnitude lower than in polycrystalline metallic systems[11,35,36]. Comparable speeds to those observed here have previously been reported in synthetic

antiferromagnets[36] and metallic ferrimagnets at angular momentum compensation[37], but at significantly higher current densities. These results show that pure spin current from the spin Hall effect can drive homochiral DWs at very high speeds using modest current densities in insulating magnetic oxides.

Figure 5b shows that v varies linearly with H_x as expected for chiral Néel DWs driven by damping-like torque. The field at which the extrapolated velocity vanishes is ~50 Oe, which corresponds to H_{DMI}, in agreement with our depinning measurements (Fig. 3). Hence, the DMI plays a critical role in the current-driven DW dynamics; however, the fast velocities cannot be accounted for the DMI strength alone. In ferromagnets, DWs driven by damping-like spin-orbit torque exhibit a maximum velocity proportional to the DMI strength, which for the present material parameters (see Methods) would correspond to just a few tens of m/s (Fig. 5c). However, for ferrimagnets, antiferromagnetic coupling of the sublattices leads to an inhibition of the DW plane precession that is responsible for the velocity saturation[36,37]. As described in Ref.[37], in ferromagnets, the DW velocity can be written $v(j) = \frac{\pi\gamma\Delta}{2\alpha} H_{DL} / \sqrt{(1 + (H_{DL}/\alpha H_{DMI})^2)}$, which tends to saturate for $H_{DL} \sim \alpha H_{DMI}$, with damping-like effective field $H_{DL} \propto j$ and DMI effective field $H_{DMI} \propto D$. For ferrimagnets, the DW dynamics can be accurately modelled by re-scaling the gyromagnetic ratio γ and damping constant α to yield an equation of motion for the Néel vector, which takes into account the collective dynamics of two antiparallel sublattices. Following that approach (see Methods), we predict a qualitatively similar dynamics (Figs. 5c,d) to what we observe experimentally, showing that despite the relatively weak DMI, very fast DW speeds can be attained. In particular, since α is re-scaled by a factor $\left(\frac{M_{S,1}}{\gamma_1} + \frac{M_{S,2}}{\gamma_2}\right) / \left(\frac{M_{S,1}}{\gamma_1} - \frac{M_{S,2}}{\gamma_2}\right) \approx 500$ for these material parameters (where the subscripts refer to the antiparallel sublattices, see Methods), much higher velocities can be attained since velocity saturation occurs at a much higher current density. Moreover, this

implies that by tuning, e.g., α it is possible to further increase the DW velocity at a given current density.

In conclusion, we report a chiral exchange field in centrosymmetric thin-film rare-earth iron garnets that stabilizes Néel DWs with a fixed chirality. We show that spin currents generated by charge current in an adjacent Pt layer can be used to exert substantial damping-like torque on these DWs, leading to efficient current-induced motion at zero applied field. We find small critical currents of a few 10^{10} A/m^2, which we attribute to the high-quality crystalline nature of these materials leading to a low density of defects. Combined with a high current-driven mobility enabled by antiferromagnetic spin dynamics, this allows for fast DW motion at modest current densities, with speeds ~800 m/s per $j \cong 1.2 \times 10^{12}$ A/m^2. These attributes make rare-earth iron garnets promising for low-power, high-speed DW motions. We find that the interfacial DMI persists whether Pt is in direct contact with the film or not, and occurs generally in a family of RE garnets, and we suggest that it may originate at the substrate oxide-oxide interface by a Rashba-type spin-orbit interaction. The possibility to achieve chiral magnetism in magnetic insulators and efficient manipulation of chiral textures by pure spin currents marks an important advance in oxide-based spin-orbitronics.

Acknowledgments

This work was supported by the DARPA TEE program. We thank Dr. Luqiao Liu for use of ion milling equipment. C.O.A. thanks Aik Jun Tan for fruitful discussions.

Author Contributions

C.O.A., C.A.R. and G.S.D.B. conceived the project and planned the experiments; E.R. synthesized and characterized the TmIG and TbIG samples; C.O.A. deposited the metal layers and micro-fabricated the domain wall tracks; C.O.A., L.M.C., M.M., C.M., and D.B. prepared the experimental setup; C.O.A. and L.M.C. performed the measurements; L.M.C. and F.B.

modeled the domain wall dynamics. C.O.A. and G.S.D.B. analyzed the data and wrote the manuscript. All authors contributed to the discussion of the data in the manuscript and Supplementary Information.

Competing financial interests

The authors declare no competing financial interests.

Methods

Materials growth, characterization, and device patterning. TmIG(5.1 nm) and TbIG(7.1 nm) films were deposited on $Gd_3Ga_5O_{12}$ (111) single-side polished substrates by pulsed laser deposition (PLD) using 248 nm KrF excimer laser with 10 Hz repetition rate. The targets were prepared from Fe_2O_3 and Tm_2O_3 or Tb_2O_3 powder by a mixed oxide sintering method. Before and during deposition, the substrate holder was heated to a setpoint temperature of 900°C, corresponding to a substrate temperature of 650°C, in an oxygen atmosphere of 150 mTorr. The target-sample distance was 8 cm and the cooling rate of the chamber after deposition was 10 °C/min. These conditions yield films with an excess of rare-earth (RE:Fe approximately 0.7) and the TbIG compensation temperature is ~330 K, higher than bulk (~250 K). The origin of this discrepancy may be off-stoichiometry and/or antisite defects and ions in valence states other than 3+ which is changing the magnetization on the sublattices. This would lead to ions in the unexpected sites (e.g. Tb^{3+} is known to transition to Tb^{4+}, a stable $4f^7$ ion, in order to enter octahedral sites) creating an imbalance between the sublattices compared to ideal TbIG. Epitaxial growth of the films was confirmed via a high-resolution x-ray diffraction 2θ-ω scan of the (444) reflection. Film thicknesses were determined by x-ray reflectometry. Atomic force microscopy measurements indicated a root-mean-square roughness of less than 1 nm taken over a 1 μm^2 area for all used samples.

The films have a perpendicular easy axis due to magnetoelastic anisotropy arising from epitaxial growth on the $Gd_3Ga_5O_{12}$ substrate. TmIG is under in-plane tensile strain with a negative magnetostriction coefficient λ_{111}; TbIG is under in-plane compression with a positive λ_{111}. The room temperature saturation magnetization of the TmIG and TbIG films were 60 and 20 emu·cm^{-3}, respectively, measured using vibrating sample magnetometry. The effective perpendicular anisotropy field was determined from the field required to saturate the magnetization in-plane in SMR measurements (Fig. 1b), and corresponded to ~1 kOe for the TmIG film. The SMR signal did not saturate for TbIG for in-plane fields up to 20 kOe due to its higher perpendicular anisotropy near the compensation temperature.

Metallic overlayers (Pt and Cu/Pt) were deposited by d.c. magnetron sputtering at room temperature with base pressure $< 3 \cdot 10^{-7}$ Torr and the deposition rate of ~2 nm/minute. Film thicknesses were determined using a calibrated deposition rate.

Standard photolithography followed by Ar^+ ion milling was used to define micrometer-sized domain wall track mesa structures with varying widths (10-80 μm) and lengths (50-200 μm). The contact pads and the nucleation wire were defined in a second lithography step followed by Ta(5 nm)/Au(60 nm) deposition and lift-off.

Electrical setup and measurements. Hall effect measurements reported in Fig. 1 were performed on 20 μm-wide and 200 μm-long devices by injecting an a.c. current with amplitude $I_{RMS} = 2$ mA and frequency $\omega/2\pi = 3678$ Hz and measuring the Hall voltage V_ω using a lock-in amplifier. A typical device resistance was ~1 kΩ. The measured a.c. Hall voltage was converted to a Hall resistance using $R_H = \frac{V_\omega}{I}$. Current-induced switching in Fig. 1d was characterized using a procedure similar to that in Ref.[10]. Briefly, we first saturated the film and then applied a large reverse field step to determine the full-scale change in either R_H or the MOKE signal upon magnetization reversal, which was used as a reference. Then, to generate

the hysteresis loops shown, for the positive-going branch, we saturated the film in the –z direction and injected a 5 ms current pulse with a progressively-increasing amplitude, and normalized the change in R_H or MOKE signal to the full-scale value to determine the fractional change in out-of-plane magnetization at each current data point. The negative-going branch was obtained similarly after saturating in the +z direction. Each data point represents switching obtained by analyzing a signal-averaged switching transient obtained from 5 switching cycles for the Hall effect measurement, and 1000 switching cycles for the MOKE measurement, due to the lower signal-to-noise for the latter.

Magneto-optical Kerr effect (MOKE). The MOKE setup is in the polar configuration where the signal is related to the out-of-plane component of the magnetization, and the incident beam is normal to the sample plane. The light source is a continuous-wave diode laser with a wavelength of 632 nm, focused with a 10x objective and positioned relative to the sample using a high-resolution scanning stage. The laser spot size was determined using a knife-edge technique by scanning it over the edge of a lithographically-defined Pt pad and fitting the measured reflectivity profile to an error function. The laser spot had a 1/e full-width of 4.9 μm. Due to the low signal to noise, MOKE switching measurements were obtained by signal-averaging on the order of 1000 reversal transients.

Field/Current-induced domain wall propagation. In order to determine the field-induced domain wall velocity, the magnetization was first saturated along the **–z (+z)** direction and then an out-of-plane driving field $+H_z$ ($-H_z$) below the coercive field was applied. A short current pulse (I_{nuc}) was then injected along the Au wire at time $t = 0$ such that the local Oersted field nucleates a reverse domain, which expands under H_z. The MOKE signal was monitored at a distance d from the nucleation line to detect passage of the propagating DW as shown in Fig.2a of the main text. For the current-induced domain wall propagation we nucleated a reverse

domain by applying I_{nuc} along the nucleation wire and subsequently we send current pulses of variable amplitude along the track to move the DW. In order to determine the DW speed reported in Fig.5, we injected a series of short current pulses to drive it along the track and across the MOKE probing laser spot. The driving sequence was repeated at two probing positions and the velocity was taken as the ratio of the distance between the two locations and the cumulative pulse injection time between switching measured at the two locations.

Critical current measurements. The measurements of critical current j_{crit} versus in-plane field H_x in Fig. 3c were obtained as follows. For up-down domain walls, a reversed domain was prepared as explained above. The MOKE spot was placed along the track away from the Au nucleation line, and a 70 μs long current pulse was injected in the presence of a bias field H_x while the MOKE signal was recorded. The current amplitude of the pulse was progressively increased until switching was observed, and this threshold current was taken as the switching current. Then, we determined whether the same current density was capable of switching the local magnetization in the absence of initial domain nucleation, which would imply that reversal was through current-induced spin-orbit torque switching rather than domain wall propagation. Such data points were excluded from the data plotted in Fig. 3c, so that those data represent current-driven depinning thresholds rather than current-induced switching.

Model calculations and simulation parameters. We numerically solved the 1D model of SOT-driven domain wall motion for the case of a ferromagnet, and for a ferrimagnet in the case of strongly coupled (fully antiparallel) sublattices, following the model described in Ref. 26. We set the sublattice magnetizations to $M_{s1} = 3.3 \times 10^5$ A/m (tetrahedral Fe^{3+} sublattice) and $M_{s2} = 2.7 \times 10^5$ A/m (octahedral Fe^{3+} and Tm^{3+}) respectively, based on the bulk site occupancies in TmIG, yielding a net $M_s = 6 \times 10^4$. We considered $\gamma_1 = 2$ for the tetrahedral Fe^{3+} sublattice, and $\gamma_2 = 1.63$ for the average gyromagnetic ratio of the octahedral Fe^{3+} and Tm^{3+}.

We used $\alpha = 0.002$, a domain wall width $\Delta = 27$ nm, and set $H_{DMI} = 47$ Oe and $H_{DL} = 15.5$ Oe per 1×10^{11} A/m^2, as determined experimentally. To model ferromagnetic DW dynamics, the following scaling was applied[37]:

$$\gamma \rightarrow \gamma' = \frac{M_s}{S} \tag{1}$$

$$\alpha \rightarrow \alpha' = \frac{S_0}{S} \tag{2}$$

with

$$M_s = \left|M_{s,1} - M_{s,2}\right| \tag{3}$$

$$S = \left|\frac{M_{s,1}}{\gamma_1} - \frac{M_{s,2}}{\gamma_2}\right| \tag{4}$$

$$S_0 = \alpha_0 \left(\frac{M_{s,1}}{\gamma_1} + \frac{M_{s,2}}{\gamma_2}\right), \tag{5}$$

where subscripts denote sublattices.

Data availability

The data that support the findings of this study are available from the corresponding author upon reasonable request.

Additional Information

Supplementary information is available in the online version of the paper. Reprints and permission information is available online at www.nature.com/reprints. Correspondence and request for materials should be addressed to G.S.D.B.

References

1. Yamada, H. *et al.* Engineered interface of magnetic oxides. *Science* **305,** 646–648 (2004).

2. Caviglia, A. D. *et al.* Tunable Rashba Spin-Orbit Interaction at Oxide Interfaces. *Phys.*

Rev. Lett. **104,** 126803 (2010).

3. Banerjee, S., Erten, O. & Randeria, M. Ferromagnetic exchange, spin-orbit coupling and spiral magnetism at the LaAlO 3/SrTiO 3 interface. *Nat. Phys.* **9,** 626–630 (2013).

4. Bhattacharya, A. & May, S. J. Magnetic Oxide Heterostructures. *Ann. Rev. Mater. Res.* **44,** 65–90 (2014).

5. Bibes, M. & Barthélémy, A. Oxide spintronics. *IEEE Trans. Electron. Dev.* **54,** 1003–1023 (2007).

6. Kajiwara, Y. *et al.* Transmission of electrical signals by spin-wave interconversion in a magnetic insulator. *Nature* **464,** 262–266 (2010).

7. Chumak, A. V, Vasyuchka, V. I., Serga, A. A. & Hillebrands, B. Magnon spintronics. *Nat. Phys.* **11,** 453 (2015).

8. Nakayama, H. *et al.* Spin Hall magnetoresistance induced by a nonequilibrium proximity effect. *Phys. Rev. Lett.* **110,** 206601 (2013).

9. Cornelissen, L. J., Liu, J., Duine, R. A., Youssef, J. Ben & Van Wees, B. J. Long distance transport of magnon spin information in a magnetic insulator at room temperature. *Nat. Phys.* **11,** 1022–1026 (2015).

10. Avci, C. O. *et al.* Current Induced Switching in a Magnetic Insulator. *Nat. Mater.* **16,** 309–314 (2017).

11. Ryu, K., Thomas, L., Yang, S. & Parkin, S. Chiral spin torque at magnetic domain walls. *Nat. Nanotech.* **8,** 527–533 (2013).

12. Emori, S., Bauer, U., Ahn, S.-M., Martinez, E. & Beach, G. S. D. Current-driven dynamics of chiral ferromagnetic domain walls. *Nat. Mater.* **12,** 611–616 (2013).

13. Torrejon, J. *et al.* Interface control of the magnetic chirality in CoFeB/MgO heterostructures with heavy-metal underlayers. *Nat. Commun.* **5,** 4655 (2014).

14. Mühlbauer, S. *et al.* Skyrmion lattice in a chiral magnet. *Science* **323,** 915–919 (2009).

15. Yu, X. Z. *et al.* Near room-temperature formation of a skyrmion crystal in thin-films of the helimagnet FeGe. *Nat. Mater.* **10,** 106–109 (2011).

16. Seki, S., Yu, X. Z., Ishiwata, S. & Tokura, Y. Observation of Skyrmions in a Multiferroic Material. *Science* **336,** 198–201 (2012).

17. Bode, M. *et al.* Chiral magnetic order at surfaces driven by inversion asymmetry. *Nature* **447,** 190–193 (2007).

18. Thiaville, A., Rohart, S., Jue, E., Cros, V. & Fert, A. Dynamics of Dzyaloshinskii domain walls in ultrathin magnetic films. *Eur. Lett.* **100,** 57002 (2012).

19. Fert, A., Cros, V. & Sampaio, J. Skyrmions on the track. *Nat. Nanotech.* **8,** 152–156 (2013).

20. Yang, H. *et al.* Significant Dzyaloshinskii-Moriya interaction at graphene-ferromagnet interfaces due to the Rashba effect. *Nat. Mater.* **17,** 605–609 (2018).

21. Woo, S. *et al.* Observation of room-temperature magnetic skyrmions and their current-driven dynamics in ultrathin metallic ferromagnets. *Nat. Mater.* **15,** 501–506 (2016).

22. Boulle, O. *et al.* Room-temperature chiral magnetic skyrmions in ultrathin magnetic nanostructures. *Nat. Nanotech.* **11,** 449–454 (2016).

23. Jiang, W. *et al.* Blowing magnetic skyrmion bubbles. *Science* **349,** 283–286 (2015).

24. Ryu, K., Yang, S., Thomas, L. & Parkin, S. S. P. Chiral spin torque arising from proximity-induced magnetization. *Nat. Commun.* **5,** 3910 (2014).

25. Matsuno, J. *et al.* Interface-driven topological Hall effect in SrRuO3-SrIrO3 bilayer. *Sci. Adv.* **2,** e1600304 (2016).

26. Ohuchi, Y. *et al.* Electric-field control of anomalous and topological Hall effects in oxide bilayer thin film. *Nat. Commun.* **9,** 213 (2018).

27. Wang, L. *et al.* Ferroelectrically tunable magnetic skyrmions in ultrathin oxide heterostructures. *Nat. Mater.* **17,** 1087–1094 (2018).

28. Kan, D., Moriyama, T., Kobayashi, K. & Shimakawa, Y. Alternative to the topological interpretation of the transverse resistivity anomalies in SrRuO3. *Phys. Rev. B* **98,** 180408(R) (2018).

29. Gerber, A. Interpretation of experimental evidence of the topological Hall effect. *Phys. Rev. B* **98,** 214440 (2018).

30. Emori, S. *et al.* Spin Hall torque magnetometry of Dzyaloshinskii domain walls. *Phys. Rev. B* **90,** 1–13 (2014).

31. Lemesh, I., Büttner, F. & Beach, G. S. D. Accurate model of the stripe domain phase of perpendicularly magnetized multilayers. *Phys. Rev. B* **95,** 174423 (2017).

32. Heide, M. & Bihlmayer, G. Dzyaloshinskii-Moriya interaction accounting for the orientation of magnetic domains in ultrathin films: Fe/W(110). *Phys. Rev. B* **78,** 140403 (2008).

33. Veit, M. J., Arras, R., Ramshaw, B. J., Pentcheva, R. & Suzuki, Y. Nonzero Berry phase in quantum oscillations from giant Rashba-type spin splitting in LaTiO3/SrTiO3heterostructures. *Nat. Commun.* **9,** 1458 (2018).

34. Banerjee, S., Rowland, J., Erten, O. & Randeria, M. Enhanced stability of skyrmions in two-dimensional chiral magnets with rashba spin-orbit coupling. *Phys. Rev. X* **4,**

031045 (2014).

35. Miron, I. M. *et al.* Fast current-induced domain-wall motion controlled by the Rashba effect. *Nat. Mater.* **10,** 419–423 (2011).

36. Yang, S., Ryu, K. & Parkin, S. Domain-wall velocities of up to 750 m s − 1 driven by exchange-coupling torque in synthetic antiferromagnets. *Nat. Nanotech.* **10,** 221–226 (2015).

37. Caretta, L. *et al.* Fast current-driven domain walls and small skyrmions in a compensated ferrimagnet. *Nat. Nanotech.* **13**, 1154-1160 (2018).

Figures

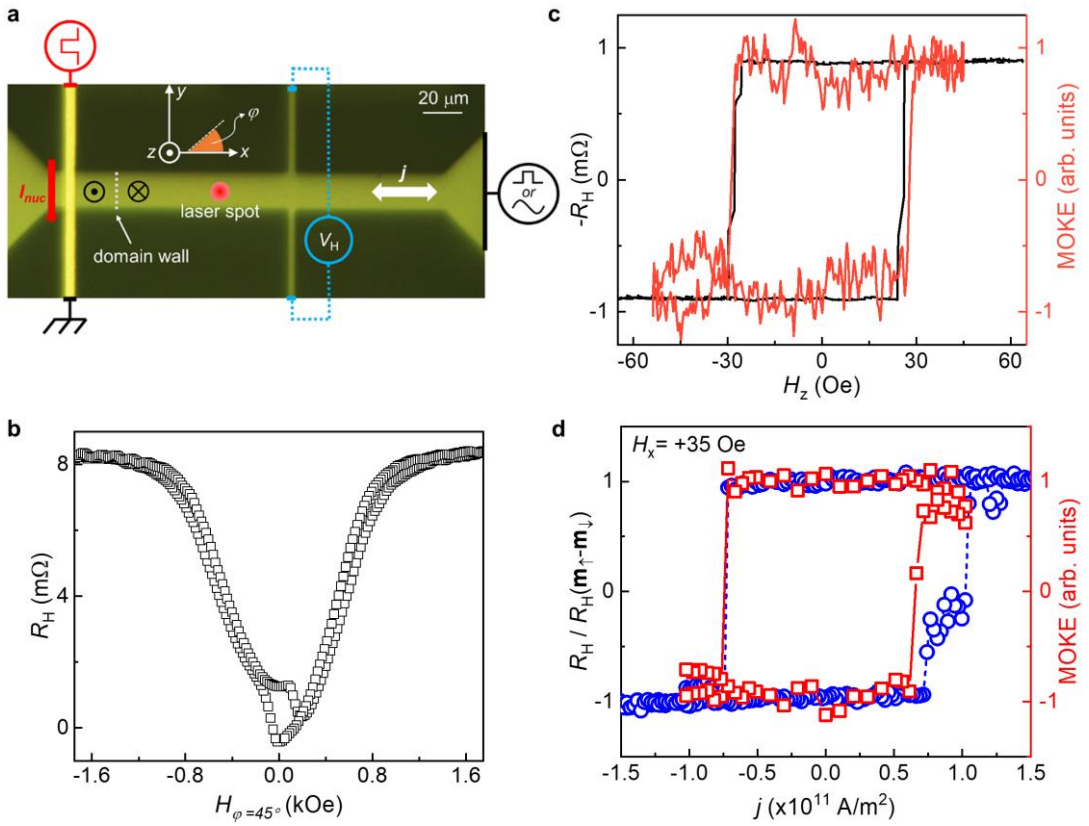

Figure 1 – **Experimental setup and the current-induced magnetization reversal. a,** Optical micrograph of a domain wall track with schematically-indicated electrical connections, and definition of coordinate system and the in-plane angle. The black region is the substrate, the dark yellow region is the TmIG/Pt bilayer track, and the vertical bright yellow line is the DW nucleation wire. Thick red and white arrows show the direction of the nucleation (I_{nuc}) and domain wall drive currents. A schematic depiction of the domain configuration is shown near the nucleation wire after injection of I_{nuc} for magnetization initially saturated along –z. **b,** Hall resistance R_H measured while sweeping an in-plane field (H_{IP}) at $\varphi_H = 45°$, corresponding to the spin Hall magnetoresistance. **c,** Out-of-plane hysteresis loop measured using the anamolous Hall-like signal (black curve) and the polar magneto-optical Kerr effect (MOKE) measured near the center of the track. **d.** Current-induced switching probed electrically (through R_{H}) and by MOKE.

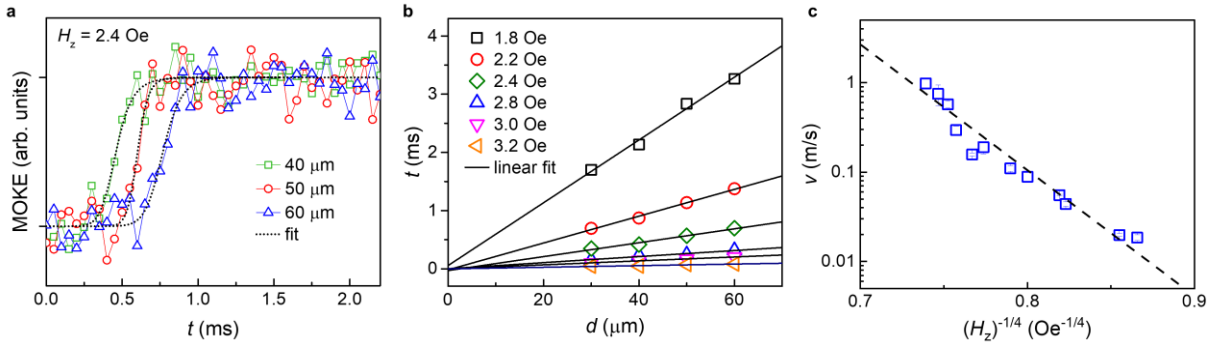

Figure 2 – Field-driven domain wall dynamics. a, Time-resolved MOKE reversal transients measured at several distances from the Au nucleation wire, for a driving field H_z = 2.4 Oe, fitted by an error function to determine the mean domain wall arrival time. Here, the magnetization was first saturated along the –z direction and then an out-of-plane driving field H_z below the coercive field was applied. A short current pulse was then injected along the Au wire at time t = 0 such that the local Oersted field nucleates a reverse domain, which expands under H_z. The MOKE signal was monitored at a distance d from the nucleation line to detect passage of the propagating DW. **b,** Domain wall arrival time versus position, extracted by fitting the MOKE transits with an error function, with d = 0 corresponding to the position of the Au nucleation line, along with linear fits whose slope is used to extract the mean velocity. **c,** Domain wall velocity v as a function of driving field H_z plotted for creep scaling. A small field offset from the earth's magnetic field was determined by comparing measurements at positive and negative H_z and was used to correct the driving field plotted in the horizontal axis in **c**.

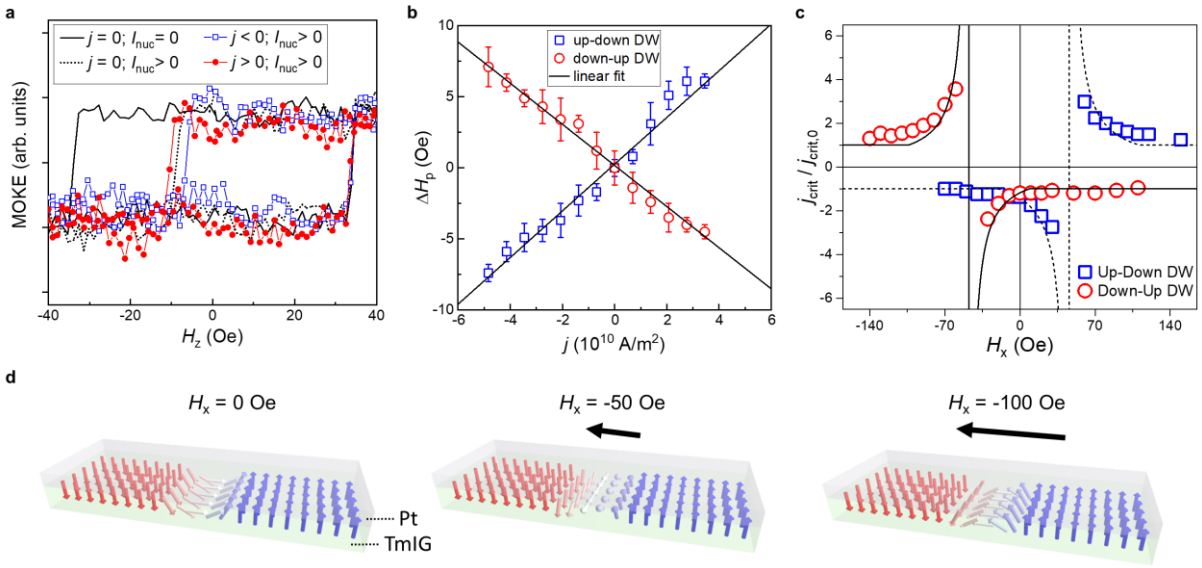

Figure 3 –Current-assisted depinning and domain wall propagation. a, MOKE signal in the absence (continuous black line) and presence (dotted gray line) of nucleation pulses injected along the Au nucleation line at the zero-field crossing of the positive-going field sweep half-cycle. The influence of positive (red curve) and negative (blue curve) current injection along the track (current density j) after domain nucleation. The magnetization switching that occurs at around $H_z \sim 30$ Oe corresponds to domain nucleation, whereas the switching around $H_z \sim -10$ Oe corresponds to domain wall propagation. **b,** Change in the domain wall propagation field (ΔH_p) as a function of j, for up-down and down-up domain walls. Error bars represent the uncertainty in estimating the switching field given the finite signal-to-noise ratio of the MOKE signal. **c,** Critical current (j_{crit}) normalized by the critical current obtained at $H_x = 0$ Oe, for domain wall depinning for up-down and down-up domain walls as a function of in-plane field H_x. Error bars were computed by repeating each measurement 5 times and computing the standard deviation, and are approximately the size of the symbols used in the figure and so are omitted. **d,** Schematic representation of the behavior of a Dzyaloshinskii-Moriya stabilized Néel domain wall in the presence of an increasing field H_x oriented antiparallel to its internal moment.

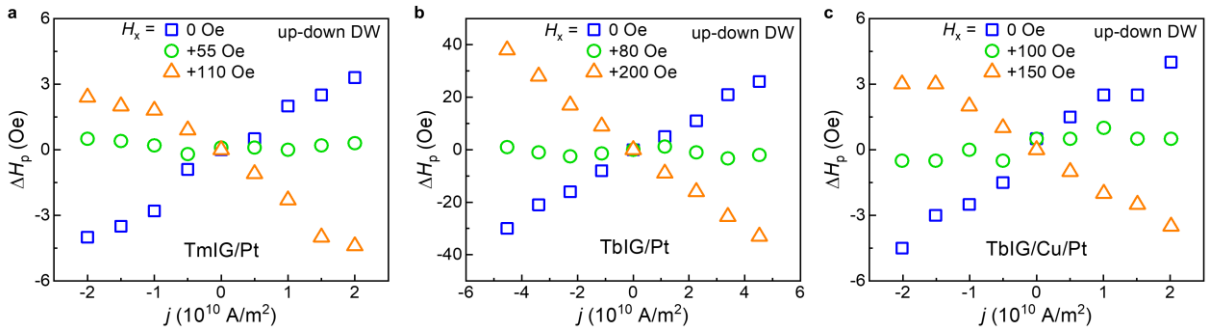

Figure 4 – Measuring chiral exchange fields for various RE garnets and interfaces. Measurement of the change in domain wall propagation fields as a function of current density j, similar to the measurement in Fig. 3b, for **a,** TmIG(5.1 nm)/Pt(4nm), **b,** TbIG(7.1 nm)/Pt(4nm), and **c,** TbIG(7.1 nm)/Cu(2 nm)/Pt(4 nm). Measurements shown are for the case of an up-down domain wall, under zero applied field, with an applied field H_x that reduces the slope to zero (corresponding to the DMI effective field), and for a larger negative H_x that reorients the Néel domain wall to the opposite chirality, inverting the slope.

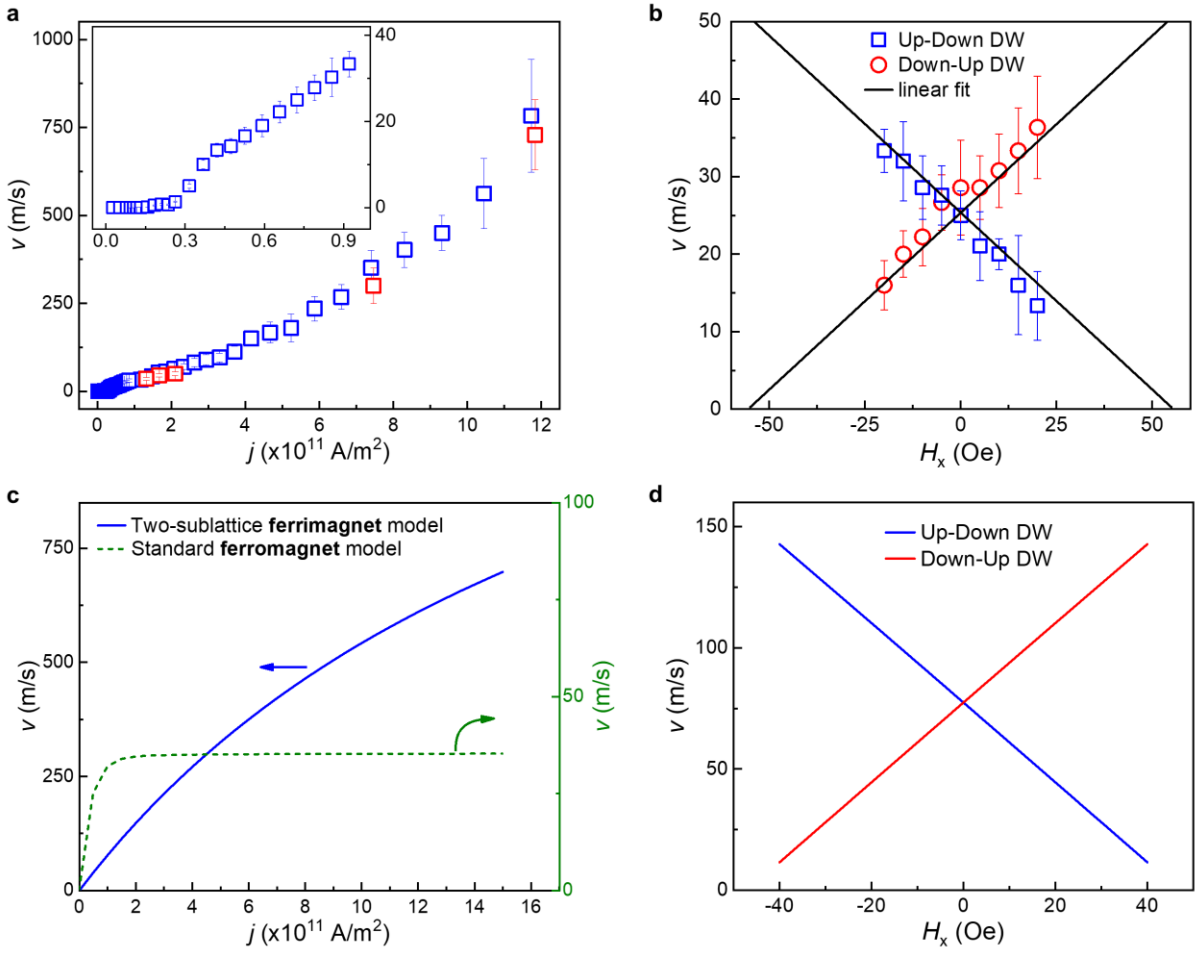

Figure 5 – Current-driven domain wall velocity. a, Domain wall velocity (v) versus current density (j) for TmIG/Pt; inset shows the region around the critical depinning threshold. Blue and red data points correspond to independent measurements on two different devices fabricated from the same film. **b**, v versus H_x measured at a current density $j = 1 \times 10^{11}$ A/m^2 for up-down and down-up domain walls. Linear fits extrapolated to $v = 0$ yield the DMI effective field. Error bars were computed from the error in the domain wall transit times between two MOKE probe points, based on the uncertainty of an error function fit to the MOKE reversal transients. **c**, Model calculations of v versus j in the case of two-sublattice ferrimagnet model (left y-axis) and standard ferromagnetic model (right y-axis). A quasi-linear non-saturating velocities are found in the former, whereas in the latter the velocity increases initially and quickly saturates around $j \sim 1.5 \times 10^{11}$ A/m^2. **d**, Model calculations of v versus H_x with a fixed current density of $j = 1 \times 10^{11}$ A/m^2 in the case of two-sublattice ferrimagnet model for

up-down and down-up domain walls. Please see text for details regarding the model and the parameters used.